

Logical Error Rates for a $[[4,2,2]]$ -encoded Variational Quantum Eigensolver Ansatz*

Meenambika Gowrishankar[†]

*Bredesen Center for Interdisciplinary Research and Graduate Education,
University of Tennessee, Knoxville, TN, USA and
Quantum Science Center, Oak Ridge National Laboratory, Oak Ridge, TN, USA*

Daniel Claudino

*Quantum Information Science Section, Oak Ridge National Laboratory, Oak Ridge, TN, USA and
Quantum Science Center, Oak Ridge National Laboratory, Oak Ridge, TN, USA*

Jerimiah Wright

Quantum Information Science Section, Oak Ridge National Laboratory, Oak Ridge, TN, USA

Travis Humble

*Bredesen Center for Interdisciplinary Research and Graduate Education, University of Tennessee, Knoxville, TN, USA
Quantum Information Science Section, Oak Ridge National Laboratory, Oak Ridge, TN, USA and
Quantum Science Center, Oak Ridge National Laboratory, Oak Ridge, TN, USA*

(Dated: January 15, 2025)

Quantum computing offers a potential for algorithmic speedups for applications, such as large-scale simulations in chemistry and physics. However, these speedups must yield results that are sufficiently accurate to predict realistic outcomes of experiments precisely. Delivering on the promise of high accuracy and precision requires methods to evaluate the computational accuracy of the quantum computing devices. We develop a framework to estimate the computational accuracy of near-term noisy, intermediate scale quantum (NISQ) computing devices using a quantum chemistry application. Application benchmarks that run on NISQ devices require techniques for mitigating errors to improve accuracy and precision. We use device agnostic error-mitigation schemes, quantum error detection and readout error detection, with post-selection to mitigate the dominant sources of noise. We evaluate the framework by simulating the ground state of molecular hydrogen with the variational quantum eigensolver (VQE) algorithm, estimating the energy and calculating the precision of the estimate using numerical simulations with realistic noise models. We first quantify the improvement in the logical error rate and state fidelity of the VQE application when encoded with the $[[4,2,2]]$ quantum error detection code. When additionally encoded with readout error detection, we show that compared to the unencoded simulation, the encoded simulation yields a more accurate estimate by more than 1 mHa (0.027 eV) with comparable precision and higher state fidelity. Additionally, unlike the best estimate from the unencoded simulations, the results from the encoded simulation fall within the chemical accuracy threshold of 1.6 mHa of the exact energy. The estimated accuracy and precision indicate that current quantum computers can achieve error rates that yield useful outcomes for chemical applications.

I. INTRODUCTION

Quantum computing hardware has made remarkable strides in improving the coherence times of qubits and the fidelity of gates with error rates in state-of-the-art devices around 0.5 – 0.01% per two-qubit gate [1–3]. Error rates required for implementing large scale quantum

computations are much lower at $\sim 10^{-9}$, which is considered extremely challenging to achieve on hardware [4]. Lower error rates are made possible by the application of quantum error correction (QEC), which involve redundantly encoding logical qubits using a larger number of physical qubits such that errors can be detected, decoded and corrected during the computation [5–8]. The leading QEC codes that promise such error rates at physical gate error of 0.1% are the surface code and quantum low-density parity-check (LDPC) codes [9, 10]. However, successfully implementing these error correction codes on near-term devices for fault-tolerant quantum algorithms remains an ongoing area of research [1, 11–16].

Quantum error detection (QED) codes, on the other hand, can be implemented on current quantum computers. Unlike QEC, QED uses encoded data qubits only to identify if an error occurred and does not require syndrome decoding or feed-forward operations for its implementation. For example, the $[[4,2,2]]$ QED code uses 4

* This manuscript has been authored in part by UT-Battelle, LLC under contract DE-AC05-00OR22725 with the U.S. Department of Energy. The United States Government retains and the publisher, by accepting the article for publication, acknowledges that the United States Government retains a non-exclusive, paid-up, irrevocable, world-wide license to publish or reproduce the published form of this manuscript, or allow others to do so, for United States Government purposes. The Department of Energy will provide public access to these results of federally sponsored research in accordance with the DOE Public Access Plan (<http://energy.gov/downloads/doe-public-access-plan>).

[†] Contact Author: mgowrish@vols.utk.edu

physical qubits to encode 2 logical qubits and detects at most one physical qubit error [8]. While QED does not enable fault tolerant operations, post-selection of the flagged measurement results can be used to improve the accuracy of calculated outcomes.

QED codes have been studied extensively both theoretically and experimentally [17–30]. Most experiments to date have focused on demonstrating that QED codes can successfully detect errors during state preparation [21, 22, 25, 29], while others have tested early fault tolerance on near-term devices [24, 26–28]. The $[[4,2,2]]$ code and its variant $[[4,1,2]]$ code have been at the center of most of these studies. Several studies have reported on improvements during state preparation, while others have demonstrated the use for applications [3, 31, 32]. These encoded applications include using the $[[4,2,2]]$ QED code with the variational quantum eigensolver (VQE) algorithm and Grover’s search algorithm, respectively [31, 32]. The former demonstrated the use of the $[[4,2,2]]$ code to encode a two-qubit ansatz for molecular hydrogen for the VQE algorithm [31]. The study showed improvement in accuracy of the ground state expectation value of the encoded hydrogen ansatz across the potential energy surface when compared to the unencoded simulation on an IBM 5Q quantum computing device. The encoding employs a circuit construction introduced in [23] that uses an ancilla and a destructive parity measurement to construct state preparation circuits for certain specific input states using the $[[4,2,2]]$ error detection code such that the qubits are fault tolerantly protected.

In this work, we build upon the results in [31] by developing a framework using classical error detection in addition to QED for effectively managing errors on near-term quantum computers and demonstrate results within the domain specific accuracy threshold. We use ‘chemical accuracy’ as a useful benchmark to evaluate the computational accuracy and error estimates of a near-term quantum computer in applications of computational chemistry. Chemical accuracy is defined in practice to be within 1.6 mHa of the full configuration interaction (FCI) energy for the chosen one-particle basis set and is necessary for making reliable predictions about the properties derived from these estimates, such as atomization energies and reaction enthalpies [33]. Many studies have reported average energy estimates close to or within chemical accuracy for molecular hydrogen using VQE [34–36], however, the precision of these estimates is unclear. We estimate the error rate at which both accuracy and precision of the energy are within chemical accuracy when using this encoding in comparison to the unencoded simulation of the ground state of molecular hydrogen. A recent study reported energy estimates with both accuracy and precision within chemical accuracy for ground state of molecular hydrogen for both the unencoded and the $[[4,2,2]]$ -encoded ansatz on a Quantinuum device [37]. Among the key differences between their framework and ours is their use of a different ansatz, use of additional methods such as classical shadows and sim-

ulation of twice the number of samples of the $[[4,2,2]]$ -encoded ansatz as the unencoded ansatz for calculating the energy estimates.

II. BACKGROUND

This section presents an overview of the VQE algorithm for estimating the energy of a molecular Hamiltonian with chemical accuracy. We then review how to apply the encoding methods defined by the $[[4,2,2]]$ code and the repetition code for creating the variational ansatz state before discussing methods to post-process the detection outcomes.

A. Molecular Electronic Hamiltonian

The central problem of electronic structure theory is to find the ground state of a molecule by finding the lowest eigenvalue of the electronic Hamiltonian. We start with the electronic Hamiltonian with coefficients h_{pq} and h_{pqrs} that are a function of the internuclear geometry R and is represented in the second quantized form as:

$$H(R) = \sum_{pq} h_{pq} a_p^\dagger a_q + \frac{1}{2} \sum_{pqrs} h_{pqrs} a_p^\dagger a_q^\dagger a_r a_s \quad (1)$$

where a_p^\dagger and a_q are creation and annihilation operators and follow the canonical fermionic anti-commutation relations:

$$\begin{aligned} \{a_p^\dagger, a_q\} &= \delta_{pq} \\ \{a_p, a_q\} &= 0 \end{aligned} \quad (2)$$

In the case study below, we estimate the ground state energy of the hydrogen molecule using VQE. The Hamiltonian in the minimal STO-3G basis can be presented in a two-qubit representation that considers only the spin singlet configuration [38]. Using a series of fermionic and spin transformations we arrive at the final Hamiltonian shown in Equation 3.

$$H(R) = g_0 I + g_1 Z_0 + g_2 Z_1 + g_3 Z_0 Z_1 + g_4 X_0 X_1 \quad (3)$$

Details of the transformations are presented in Appendix A.

B. Variational Quantum Eigensolver

The VQE algorithm is a method to estimate the minimal expectation value of a Hermitian operator with respect to a variable pure quantum state [39]. It is based on the variational principle from quantum mechanics, which asserts that only the lowest eigenstate, aka ground state, of a non-negative, Hermitian operator minimizes the

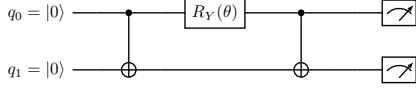


FIG. 1. The unencoded two-qubit UCC single parameter VQE ansatz.

expectation value. Estimating the energy is then described by the optimization

$$E(\theta^*) = \min_{\theta} \langle \psi(\theta) | H | \psi(\theta) \rangle \quad (4)$$

where $|\psi(\theta)\rangle = U(\theta)|\psi(0)\rangle$ is a variable pure quantum state prepared by a unitary ansatz operator $U(\theta)$ from the reference state $|\psi(0)\rangle$. The parameter θ^* denotes the optimal value obtained from minimizing the energy. The VQE reference state is typically represented by the Hartree-Fock solution to the electronic Hamiltonian. In our encoding of the hydrogen molecule above, the Hartree-Fock state corresponds to the $|00\rangle$ state.

We consider an ansatz based on unitary coupled cluster (UCC) theory which derives from the well known coupled cluster method in quantum chemistry [40–42]. The unitary operator approximated to the first Trotter step ($t = 1$) yields the UCC singles and doubles ansatz (UCCSD). In the case of molecular hydrogen, the singles excitation operator does not contribute to the energy due to Brillouin’s theorem [43]. Considering only the contribution from the double excitation T_2 , shown in Equation B2 in the appendix, we arrive at the UCC doubles (UCCD) ansatz shown in Equation 5. The transformation leading to this operator is presented in Appendix B.

$$U(\theta) = e^{-i\theta Y_0 X_1} \quad (5)$$

The circuit decomposition of Equation 5 involves the subcircuit for the $e^{-i\theta Z_0 Z_1}$ operator surrounded by single qubit rotations to perform the transformation to $e^{-i\theta Y_0 X_1}$ [44, 45]. In our encoding, some of the single qubit rotations in the decomposition are redundant for the initial Hartree-Fock input state, $|00\rangle$ and are removed. This results in the two-qubit unencoded circuit shown in Figure 1, which prepares the final state $|\chi(\theta)\rangle$ shown in Equation 6.

$$|\chi(\theta)\rangle = \cos \frac{\theta}{2} |00\rangle + \sin \frac{\theta}{2} |11\rangle \quad (6)$$

We present results for the expectation value of the Hamiltonian at the internuclear distance of 0.74\AA shown in Equation 7, where the coefficients g_i are obtained from [35].

$$H = -0.349833 \mathbb{I} - 0.388748 Z_0 - 0.388748 Z_1 + 0.0111772 Z_0 Z_1 + 0.181771 X_0 X_1 \quad (7)$$

The analytical energy expectation value and optimal parameter for this Hamiltonian and ansatz are $E(\theta^*) = -1.13712 \text{ Ha}$ and $\theta^* = -0.22967 \text{ rads}$, respectively.

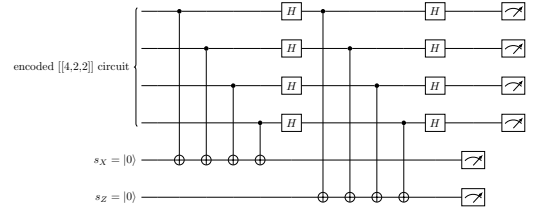


FIG. 2. Syndrome measurement circuit for the $[[4,2,2]]$ error detection code.

C. $[[4,2,2]]$ Quantum Error Detection Code

The $[[4,2,2]]$ QED code, following the $[[n, k, d]]$ convention, is a distance $d = 2$ code that encodes $k = 2$ logical qubits using $n = 4$ physical qubits. The basis states and operations for the code are provided in the Appendix C. The code can detect at most one-single physical qubit bit-flip and/or phase-flip error (Pauli X or Z error, respectively) that occurs during the encoding of the initial state [8]. The circuit for the error detection or syndrome measurement for this encoding is presented in Figure 2. Ancillas s_X and s_Z are used for error syndrome measurements and detect bit-flip and phase-flip errors, respectively.

All the basis states of this encoding have even parity (even number of 1s in the physical basis), and any single physical qubit bit-flip error will take the state outside the logical codespace and result in a state with odd parity. As a result, a single physical qubit bit-flip error will lead to a measurement of $s_X = 1$. If the state is rotated using the Hadamard ($H^{\otimes 4}$) operation before measurement, any single physical qubit phase-flip error will lead to a measurement of $s_Z = 1$. Two physical qubit bit-flip errors take the state to another logical state and will remain undetected by the ancillas. Two physical qubit phase-flip errors can add a global phase to the state or leave the state effectively unchanged.

An alternative method to observe the detectable errors is by measuring all the data qubits and selecting joint measurements based on parity. Odd parity measurements indicate that a single qubit bit-flip error has occurred and is akin to performing the stabilizer measurement with ancilla s_X in Figure 2. Similarly, odd parity of measurements made after rotating the state by applying the Hadamard ($H^{\otimes 4}$) operation indicate that a physical qubit phase-flip error has occurred and is equivalent to an $s_Z = 1$ measurement in Figure 2. The advantage of this method over the stabilizer measurement is the reduction in the number of two-qubit gates for syndrome detection. The disadvantage is that the detection of errors requires a destructive measurement and only allows detection of one of the two types of errors, a physical bit-flip or phase-flip error.

This method can be coupled with an ancilla for additional error detection during state preparation. This is applicable only to certain specific input logical states,

$|00\rangle, |0+\rangle, |0\bar{0}\rangle + |11\rangle$ and can be used during the preparation of the Hartree-Fock initial state, $|00\rangle$, in this study[23]. The ancilla detects physical qubit bit-flip errors during preparation of the input state while the parity check measurement described earlier enables detection of single physical qubit bit- or phase-flip errors.

D. Readout Error Detection (RED)

The leading single source of error in all quantum computing technologies is readout error, also called measurement error. Since the read-out error needs to be mitigated before applying the post-selection strategies associated with the $[[4,2,2]]$ -encoding, we require a readout error mitigation technique that can be applied to every shot or circuit measurement. Considering that read-out errors are comprised of only bit-flip errors, they can be managed using classical error detection codes. The classical repetition code is a method both for detecting classical bit-flip errors and to filter noisy results from every measurement prior to post-selection for the $[[4,2,2]]$ -encoded ansatz.

We consider the three-qubit repetition code referred to as $[[3,1]]$ -RED code, which encodes one logical readout qubit with three physical qubits [46]. The circuit encodes the data qubits just prior to their measurement. The data qubits are encoded by entangling each of them with two ancillas and errors are detected based on unanimous vote.

The success of the code in mitigating readout errors depends on the difference in magnitude of error rates between the two-qubit gate error and readout error. Having a much lower two-qubit gate error rate than readout error rate will lead to higher accuracy of the observable calculated from the post-selected measurements. A much lower two-qubit gate error rate would introduce much fewer errors due to the gate than the readout error, increasing the probability that the error observed during RED is due to measurement error rather than two-qubit gate error. Using the RED method with a higher two-qubit gate error rate than read-out error rate will lead to a decrease in accuracy of the results as the likelihood that the errors in measurement are caused due to the additional two-qubit gates used for the RED encoding becomes higher than errors introduced due to the measurement itself.

III. ENCODING METHODS

In this section, we present details on the methods to encode the VQE algorithm and UCCD ansatz using the $[[4,2,2]]$ code. We also review the methods used to simulate and post-process results for the electronic Hamiltonian of molecular hydrogen in the presence of circuit noise.

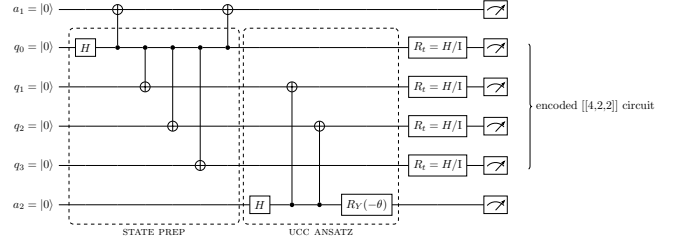


FIG. 3. The $[[4,2,2]]$ encoded ansatz for the hydrogen molecule. The block labeled 'STATE PREP' describes the circuit to prepare the initial state in the $[[4,2,2]]$ encoding. The block labeled 'UCC ansatz' describes the implementation of the UCC derived hydrogen VQE ansatz in the $[[4,2,2]]$ encoding. $R_t = H/I$ indicates the basis of the state prior to measurement, in the X or computational basis, respectively.

A. $[[4,2,2]]$ Encoding of the UCC Ansatz

The corresponding $[[4,2,2]]$ encoding of the parameterized UCC two-qubit ansatz shown in Figure 1 for simulating the hydrogen molecule is presented in Figure 3 [31]. The first block on the left, labeled "STATE PREP", represents the circuit to prepare the initial logical $|00\rangle$ state of the unencoded ansatz and can be prepared in a wide variety of ways [23, 24, 31]. The second block labeled, "UCC ANSATZ", represents the execution of the UCC ansatz in the $[[4,2,2]]$ encoding [31]. The parameterized rotation gate in the ansatz is non-transversal in this encoding and therefore, an ancilla, a_2 , is used to teleport the gate. The final state following the action of the parametrized unitary operator corresponding to the encoded circuit ($|\psi_{enc}(\theta)\rangle$) is shown in Equation 8.

$$\begin{aligned}
 |\psi_{enc}(\theta)\rangle = & \frac{1}{\sqrt{2}} [(|0\rangle_{a_1} \otimes (\cos \frac{\theta}{2} |00\rangle_{q_0-q_3} \\
 & + \sin \frac{\theta}{2} |11\rangle_{q_0-q_3}) \otimes |0\rangle_{a_2}) \\
 & + (|0\rangle_{a_1} \otimes (\cos \frac{\theta}{2} |11\rangle_{q_0-q_3} \\
 & - \sin \frac{\theta}{2} |00\rangle_{q_0-q_3}) \otimes |1\rangle_{a_2})]
 \end{aligned} \tag{8}$$

The action of this non-transversal gate in the encoded circuit results in a uniform superposition of equivalent states, each representing the unencoded final state, with equal probability to be in $a_2 = |0\rangle$ or $|1\rangle$, and with each minimizing the expectation value at a different parameter. The optimal parameter, θ^* , at $a_2 = |0\rangle$, is shifted by π when $a_2 = |1\rangle$. For the purpose of calculating expectation values, we only use outcomes with $a_2 = |0\rangle$ resulting in the final state shown in Equation 9. This excludes $\sim 50\%$ of the total number of outcomes measured, belonging to the subset with $a_2 = |1\rangle$, from our calculations. The corresponding state for $a_2 = |1\rangle$ is shown in

1. Post-Selection Strategies

We introduce and analyze several different post-selection strategies. We post-select outcomes from the measurement bitstrings once all qubits are measured. The expectation values of each Pauli term in the Hamiltonian are estimated from the available, post-selected measurements. Measurement of ancilla, $a_1 = 1$ indicates a bit-flip error has occurred on qubit q_0 . As a result, for post-selection by ancilla a_1 (PSA) measurement, we discard all measurements with $a_1 = 1$.

Since measurements of the encoded qubits/data qubits with odd parity indicate a single physical qubit bit- or phase-flip error, for post-selection by logical state parity (PSP), we discard measurement bitstrings that have odd parity but include measurement counts with both measurements of ancilla, $a_1 = 0$ and $a_1 = 1$. We also consider a post-selection strategy labeled PSAP that combines both the PSA and PSP strategies. In this post-selection method, we discard measurement outcomes that have odd parity or ancilla, $a_1 = 1$.

We also calculate the SEM for the energy estimated from each post-selection method as an estimate of the precision of the calculation.

2. Probability of Success

We report on the probability of success (POS) defined as the fraction of samples η that is retained after post-selection for each post-selection strategy. The SEM for the resulting binomial distribution for each post-selection method is calculated as

$$\sigma_{\text{POS}} = \sqrt{\frac{(1-\eta)(\eta)}{N}} \quad (12)$$

where N is the number of samples with $a_2 = 0$.

3. Logical Fidelity and Logical Error

We calculate the logical fidelity of the prepared states as generated by the noisy circuit simulations. We simulate the two-qubit UCCD ansatz state for the hydrogen molecule and the corresponding $[[4,2,2]]$ encoded circuit described in Figures 1 and 3, respectively. With the resulting final state for the encoded circuit shown in Equation 9 we use projection operators to assess the impact of each post-selection technique using fidelity. We calculate the fidelity for the PSA method by using operators Π_A to project states from the noisy state with $a_1 = |0\rangle$ and identity (\mathbb{I}) for all other qubits. For the PSP strategy, we project states within the codespace, i.e., within the states in Equation C1, using operators Π_P . And we use the operator, Π_{AP} for projecting states with $a_1 = |0\rangle$ and states within the codespace. The operators are presented in Appendix D.

We calculate the logical fidelity of the states projected using operators Π_A, Π_P, Π_{AP} , and the original encoded and unencoded states. We define the fidelity F between two states ρ_1 and ρ_2 as

$$F(\rho_1, \rho_2) = \left(\text{Tr} \sqrt{\sqrt{\rho_2} \rho_1 \sqrt{\rho_2}} \right)^2 \quad (13)$$

Here, we consider the case that $\rho_1 = |\Psi\rangle\langle\Psi|$, where $|\Psi\rangle$ is the expected ground state, i.e., the noiseless state, from the noise-free simulation and ρ_2 is the representation of the prepared, noisy unencoded, encoded or projected state. The fidelity of the projected state is calculated by $F_i(\rho_1, \rho_i)$, where $\rho_i = \frac{\Pi_i \rho_{\text{noisy}} \Pi_i^\dagger}{\text{Tr}(\Pi_i \rho_{\text{noisy}} \Pi_i^\dagger)}$ is the projected state, ρ_{noisy} is the noisy encoded state, and $\Pi_i \in \{\Pi_A, \Pi_P, \Pi_{AP}\}$. We also calculate the minimum expectation value of energy for the state ρ_i as

$$E(\theta^*) = \text{Tr}(H \rho_i(\theta^*)) \quad (14)$$

which represents an estimate in the limit of infinite samples of the measured state.

As part of the error analysis of the $[[4,2,2]]$ encoded circuit, we calculate the probability of logical error. We define logical error (p_ϵ) for the encoded circuit in Figure 3 as probability of any error that takes the target or ideal encoded logical state to a different encoded logical state. We restrict the calculation to states with $a_2 = 0$. Therefore the logical error is the probability of measuring any state within the codespace shown in Equation C1 in the Appendix other than the state $|\psi_{enc}^{a_2=0}(\theta^*)\rangle$ shown in Equation 9.

We first calculate the probability to measure the ideal state, p_{ideal} , in the noisy mixed state, ρ_{noisy} , and the probability to measure any logical state, i.e., any state in the codespace described in Equation C1.

$$p_{\text{ideal}} = \text{Tr}(\rho_{\text{noisy}} \rho_{\text{ideal}}) \quad (15a)$$

$$p_{\text{logical}} = \text{Tr}(\Pi_P \rho_{\text{noisy}}) \quad (15b)$$

From these we find the probability of any error ($p_{\epsilon_{all}}$) and probability of any non-logical error ($p_{\epsilon_{NL}}$), which is any error, single- or multi-qubit, that takes the target or ideal state, ρ_{ideal} , outside the codespace described in Equation C1.

$$p_{\epsilon_{all}} = 1 - \text{Tr}(\rho_{\text{noisy}} \rho_{\text{ideal}}) \quad (16a)$$

$$p_{\epsilon_{NL}} = 1 - p_{\text{logical}} \quad (16b)$$

The probability of any logical error to occur, p_{ϵ_L} , is then obtained by subtracting the probability of any non-logical error from the probability of any error as shown in Equation 17.

$$p_{\epsilon_L} = p_{\epsilon_{all}} - p_{\epsilon_{NL}} \quad (17)$$

We additionally calculate the impact of PSA on the logical error by replacing Π_P in Equation 15b with Π_{AP} and find probability of logical error p_{ϵ_A} in this case as:

$$p_{\epsilon_A} = \text{Tr}(\Pi_{AP} \rho_{\text{noisy}}) - \text{Tr}(\rho_{\text{noisy}} \rho_{\text{ideal}}) \quad (18)$$

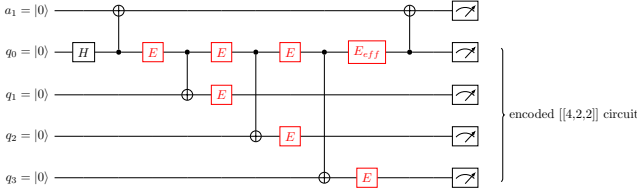


FIG. 6. Logical $|\overline{00}\rangle$ state preparation circuit for error analysis. Errors, $E \in \{X, Y, Z\}$, that can occur in the input state preparation circuit, locations are representative. Ancilla $a_1 = 1$ if $E_{eff} \in \{X, Y\}$.

4. Circuit Error Analysis

Errors detected by the PSP method are readily interpreted as single physical qubit bit-flip or phase-flip error. However, the errors detected by the a_1 in the PSA and PSAP methods require additional analysis. Errors under the depolarizing noise model we have considered include one- and two-qubit gate errors of the form E_i on qubit q_i and $E_i \otimes E_j$ on qubits q_i, q_j , respectively. Additionally, $CNOT$ gates generate two-qubit correlated errors such as a bit-flip error on the control qubit will result in a bit-flip error in the target qubit. The effective error (E'_k) after a $CNOT$ operation is applied on control qubit, i and target qubit j after an error has occurred on one of the qubits can be represented as $U_{ij}E_k|q_iq_j\rangle = E'_kU_{ij}|q_iq_j\rangle$ where $U_{ij} = CNOT_{ij}$ is the ideal operation and $E'_k = U_{ij}E_kU_{ij}^\dagger$ for $k \in \{i, j\}$. Multi-qubit errors of the form $E_1 \otimes E_2 \otimes E_3 \otimes E_4$ for $E_k \in \{X, Y, Z\}$ may also arise from concurrent one-qubit noise processes occurring on multiple qubits or from propagation of error under the two-qubit error model.

During the $[[4,2,2]]$ input state encoding, as in the section labeled “STATE PREP” in Figure 3 and shown explicitly in Figure 6, the a_1 detects any bit-flip error $E_0 \in \{X_0, Y_0\}$ that occurs on q_0 , and effectively remains a bit-flip error, $E_{eff} \in \{X_0, Y_0\}$ in Figure 6, and results in a measurement outcome for $a_1 = 1$. However, a similarly occurring phase-flip error on q_0 will not impact the a_1 and therefore, will remain undetected. Since the “STATE PREP” section is dominated by two-qubit $CNOT$ gates, there’s a high likelihood of two-qubit errors occurring in that section. Additionally, these errors may cascade into multi-qubit errors with each successive $CNOT$ gate execution as represented in Figure 6.

Based on the noise processes and resulting errors described, the discarding of the errors by a_1 , while effected by detection of bit-flip errors on q_0 , may inadvertently remove multi-qubit errors as well. Construction of the circuit such that all the $CNOT$ gates originate at q_0 with q_0 as the control ensures that many, if not most, two-qubit errors will impact q_0 . Conversely, the errors that do not affect q_0 in this “STATE PREP” section will not be detected by a_1 but the likelihood of such errors is low.

To verify whether the detection of error events by a_1 indeed enables detection of multi-qubit errors, we study

the preparation of the input logical state, $|\overline{00}\rangle$, as shown in Figure 6 under the depolarizing noise channel. We calculate the contribution towards improvement in fidelity of each post-selection method at this initial stage, when errors detected by each method are for the same final state, $|\overline{00}\rangle$, as opposed to the circuit shown in Figure 3 where the PSA method is used to detect errors during initial input state preparation and PSP at the end of the circuit. We run density matrix simulations of the circuit shown in Figure 6 for preparing the encoded logical $|\overline{00}\rangle$ state $|\phi\rangle$ shown in Equation E1 with increasing depolarizing noise and use operators to project states. Since this circuit does not include the ancilla a_2 , the projection operators differ slightly and are presented in Equation E2.

The key comparison to understand the contribution of ancilla, a_1 , is between the fidelity F_{S_P} and $F_{S_{AP}}$ of states projected by S_P and S_{AP} , respectively. Once the single qubit bit-flip errors are projected out of the prepared logical $|\overline{00}\rangle$ state, using S_P , any improvement in fidelity due to projection by S_{AP} is entirely due to the contribution of a_1 and due to detection of multi-qubit error events.

B. Realistic Hardware Noise

In addition to the study of depolarizing gate noise, we perform a similar analysis of accuracy using a realistic quantum computing hardware model. We demonstrate evaluation of the computational accuracy of a commercial device using the framework described in the previous section using the Quantinuum device emulator. We estimate the energy at the analytically determined optimal parameter with the emulator for the Quantinuum H1-1 device. The Quantinuum H1-1 device is a trapped-ion quantum charge coupled device constructed with $^{171}\text{Yb}^+$ ions as qubits and a “race-track” architecture with zones that have focused laser beams to implement gates [49]. The ions are transported to these zones for operations and the number of zones indicates the number of parallel operations possible in the device. The H1-1 device has five such zones, 20 qubits and all-to-all connectivity. The maximum number of shots that are executed for a single circuit is 10000. We accordingly perform multiple executions of 10000 shots each to reach the targeted 188000 shots and we combine the resulting measurements before estimating the results. As described in the product data sheet for the Quantinuum H1-1 emulators, the emulator is designed to closely mimic the noise profile of the device. At the time of our simulations, the version of the latest product data sheet of the emulator was 6.8.3 and was dated 18th Jul 2024. The physical noise parameters listed in this version of the data sheet are reproduced in Table I and are the parameters for the noisy simulations in this study.

The Single-qubit and Two-qubit Fault Probability are the single- and two-qubit gate noise, respectively, and are largely modeled with asymmetric depolarizing noise channels. Fractions of Single- and Two-qubit gate noise that represents spontaneous emission instead of the

TABLE I. Physical noise parameters reproduced from version 6.8.3 of the product data sheet of the Quantinuum H1-1E emulator.

Noise Parameter	Noise Value
Single-qubit Fault Probability (p1)	2.1×10^{-5}
Two-qubit Fault Probability (p2)	8.8×10^{-4}
Bit Flip Measurement Probability (0 outcome)	1.0×10^{-3}
Bit Flip Measurement Probability (1 outcome)	4.0×10^{-3}
Crosstalk Measurement Fault Probability	1.45×10^{-5}
Initialization Fault Probability	3.62×10^{-5}
Crosstalk Initialization Probability	5.020×10^{-6}
Ratio of Single-Qubit Spontaneous Emission to p1	0.54
Ratio of Single-Qubit Spontaneous Emission in Two-Qubit Gate to p2	0.43

asymmetric depolarizing noise are represented by Ratio of Single-Qubit Spontaneous Emission to p1 and Ratio of Single-Qubit Spontaneous Emission in Two-Qubit Gate to p2, respectively. The Bit Flip Measurement Probability (0 outcome) indicates probability of measuring 1 when the qubit is in 0 and vice versa for Bit Flip Measurement Probability (1 outcome). Initialization Fault Probability, as the name suggests, indicates probability of error at qubit initialization. Crosstalk error rates during measurement and initialization are indicated by Crosstalk Measurement Fault and Crosstalk Initialization Probability, respectively.

We estimate the energy at the optimal parameter for the unencoded and encoded ansatzes of molecular hydrogen on the emulator with their default error model with error parameters shown in Table I. For the simulation with the best energy estimate, we run simulations at three different parameters, $\theta \in [-0.400606, -0.22967, -0.058734]$, including the known optimal parameter $\theta^* = -0.22967$ to verify that the minimum energy estimate corresponds with the analytical optimal parameter. We calculate the energy expectation values for both the unencoded and encoded simulations, and for each post-selection method, with and without RED using $N = 188000$ shots.

For circuits with encoding for [3,1]-RED, we post-select outcomes based on unanimous vote. For each set of data and the corresponding readout qubits, a_i, k_i, l_i for $i \in [1, 2]$ and q_i, k_j, l_j for $i \in [0, 3]$ and $j \in [1, 4]$, of the $[[4,2,2]]$ -encoded ansatz as shown in Figure 5, and q_i, r_i, s_i for $i \in [0, 1]$ of the unencoded ansatz shown in Figure 4, we discard outcomes in which measurements of all three qubits in the encoding are not equal, as they indicate readout error has occurred on one or two of the qubits. For the $[[4,2,2]]$ -encoded ansatz we first post-select measurement outcomes based on RED followed by the post-selection strategies listed for the $[[4,2,2]]$ -encoding in section IV A 1. As in the case for the depolarizing error model, for each post-selection method from the simulations under the H1-1E error model we calculate the probability of success (η), and standard error of the mean as described in the previous section. We execute ansatzes in

parallel where possible. For instance, about nine circuits of the unencoded two-qubit hydrogen ansatz shown in Figure 1 can be implemented in parallel on the 20 qubit Quantinuum H1-1E device and emulator. The all-to-all connectivity proves useful for such executions.

We compare these simulated results for the expectation value of energy and accuracy against the chemical accuracy benchmark and against results from numerical simulations under the depolarizing error model. We evaluate the impact of using the $[[4,2,2]]$ QED code on hardware using the emulator and additionally compare the results against the estimates from circuits with RED to evaluate the effectiveness of the readout error encoding against the readout noise included in the emulator noise model. We then estimate the resources required to perform these simulations and compare the results between the unencoded and $[[4,2,2]]$ -encoded simulations.

V. RESULTS

We first present the results for simulations under the depolarizing error model followed by those of the Quantinuum H1-1E emulator.

A. Depolarizing Error Model

The $[[4,2,2]]$ encoded VQE circuit shown in Figure 3 and the unencoded circuit shown in Figure 1 were simulated using the IBM ‘Aer’ simulator with $N = 2 \times 10^5$ shots under a standard depolarizing noise model. All qubits were measured and the measurement counts were used to calculate expectation values of the Hamiltonian for the unencoded circuit, and the encoded circuit before and after post-selection.

The energy expectation values, variance of the calculation and probability of success at the noise parameter value at which the energy estimate reached chemical accuracy ($p = 0.09\%$) are presented in Table II. Without post-selection, the energy of the encoded ansatz is much

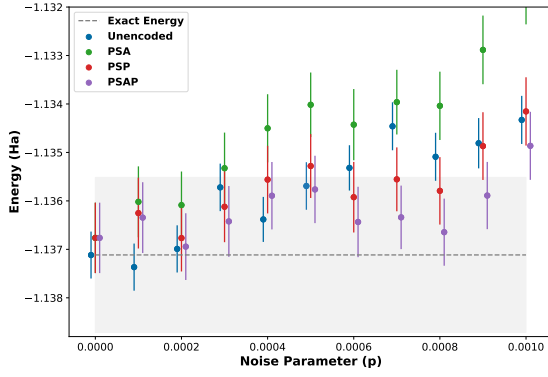


FIG. 7. Estimated energy of post-selected outcomes and unencoded simulation compared against the benchmark of chemical accuracy. Shaded region represents the region of chemical accuracy and is set to ± 1.6 mHa

higher than the unencoded ansatz and the exact energy of -1.13712 Ha. PSA improves the energy of the encoded ansatz while still falling short of the unencoded ansatz by 0.2% and PSP leads to a lower energy than PSA and the unencoded ansatz. The combined method, PSAP, reaches chemical accuracy at the highest noise parameter value of 0.09% than all other methods. PSAP leads to the highest improvement in the accuracy of the energy estimate and brings the energy estimate within chemical accuracy of 1.6 mHa.

The energy estimates at the lower end of the noise range considered are compared against the benchmark of chemical accuracy in Figure 7 for all post-selection methods. The trends are similar to those observed in Table II. The PSAP method is within chemical accuracy at noise parameters $\leq 0.09\%$ followed closely by the PSP method, which reaches chemical accuracy at $\leq 0.08\%$ noise. The trend continues even at larger noise values as shown in Figure 8. PSA improves the energy estimate over encoded ansatz simulation with no post-selection. However, it results in higher energy than the unencoded ansatz. PSP results in lower energy than both the encoded ansatz without post-selection and PSA. The results are also lower than the unencoded ansatz below noise level of 4%. Combining the two post-selection methods, PSAP results in the lowest energy and for all noise levels considered. Error bars in this plot of Figure 8 are too small to be visible and are in the range $0.06 - 2.8$ mHa.

We also present expectation value calculations using the exact density matrix for all simulations with increasing two-qubit gate noise in Figure 8. Since calculations using the exact density matrix represent estimates of the energy in the limit of infinite shots, the energy estimate from the simulations with finite number of shots should agree with the exact density matrix calculations. They are in agreement for all simulations except the calculations for the PSP and PSAP method. For both methods, energy estimated from simulations with shots is higher

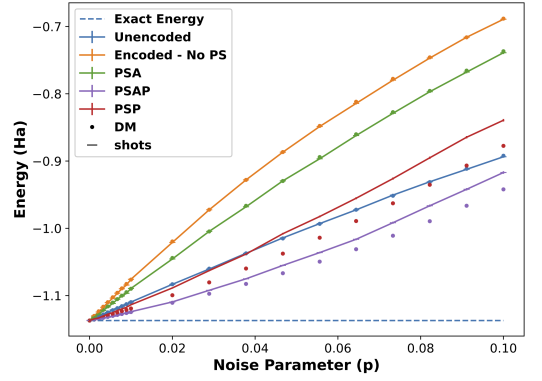


FIG. 8. Energy expectation values calculated from numerical simulations of the unencoded and $[[4,2,2]]$ encoded ansatz without (No PS) and with post-selection methods, PSA, PSP and PSAP with increasing two-qubit gate noise at 200000 shots using the IBM aer simulator and a standard depolarizing noise model.

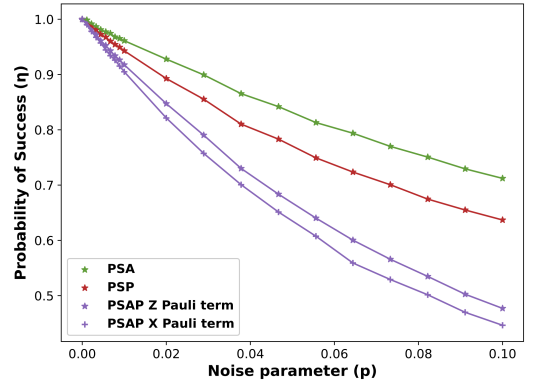


FIG. 9. Probability of success of each post-selection method, PSA, PSP and PSAP of the $[[4,2,2]]$ encoded ansatz under a standard depolarizing model. PSAP X and Z Pauli term plots are representative of the post-selection outcomes for circuits with and without the Hadamard rotation applied prior to measurement on all the encoded qubits ($q_0 - q_3$) in Figure 3, respectively. Trends between the two Pauli terms are similar for all post-selection methods.

than calculations using the exact density matrix.

The consequence of post-selection is having fewer samples for calculating energy expectation values. In all cases, including the noiseless case, since we are only considering half of the samples from the uniform superposition of the final state due to non-transversal rotation by ancilla a_2 , i.e., only samples with $a_2 = |0\rangle$, we start with $\sim 50\%$ of the original number of shots prior to implementation of any post-selection method due to detection of errors. We present the change in probability of success after each post-selection method with increasing noise in Figure 9, and in Table II, for a specific noise parameter value, normalized after selecting samples with $a_2 = |0\rangle$.

For all post-selection methods, the probability of success decreases with increasing noise indicating an in-

TABLE II. Comparing outcomes of the numerical simulations of the unencoded and $[[4,2,2]]$ encoded ansatzes with and without post-selection at 0.09% depolarizing noise parameter value and $N = 2 \times 10^5$ shots.

	Energy (mHa)	Variance (mHa)	Prob. of Success (%)
Unencoded	-1134.81 ± 0.52	5.38	100
Encoded No PS	-1131.40 ± 0.72	5.10	100
PSA	-1132.88 ± 0.71	4.99	99.644 ± 0.002
PSP	-1134.87 ± 0.70	4.84	99.472 ± 0.002
PSAP	-1135.89 ± 0.69	4.76	99.232 ± 0.003

creasing proportion of states with detected errors. This proportion is also determined by the method of post-selection. PSA retains the highest proportion of samples. However, energy expectation value calculations indicate that this does not lead to an improvement over the unencoded ansatz. Post-selection by logical state parity, PSP, results in a lower probability of success than PSA, while the highest proportion of samples are discarded due to the combined post-selection method, PSAP. Standard error of the mean in the figure is too small in magnitude to be visible but ranges from 0.006% to 0.2%. There is also a difference in the probability of success depending on the Pauli term being measured as shown in Figure 9. Probability of success for X Pauli term measurements are slightly lower than for Z Pauli term measurements due to additional noise in the circuit from the Hadamard gates used to rotate the state prior to making the measurement. The PSAP X and Z Pauli term plots are representative and apply to all other post-selection methods.

The number of samples retained consequently impact the precision of the calculation. Table II shows that there is a decrease in precision/ increase in SEM of the energy estimate from the encoded simulations with and without post-selection compared to the unencoded simulation. However, the variance of the calculation for the encoded post-selected calculations are lower than the unencoded simulations and lowest for PSAP calculation, which also results in the highest accuracy of the energy estimate. The decrease in the SEM, therefore, is a result of considering only half as many samples in the calculation for the encoded ansatz as the unencoded ansatz, where the full $N = 2 \times 10^5$ samples are included in the SEM calculation.

We now present the logical fidelity of the the unencoded state, and the encoded state, without and with projections $\Pi_i \in \{\Pi_A, \Pi_P, \Pi_{AP}\}$ corresponding with post-selection methods PSA, PSP and PSAP, respectively, with increasing two-qubit depolarizing noise p in Figure 10. The logical fidelity decreases with increasing noise, and changes with each post-selection strategy. The state fidelity of the unencoded ansatz F_{unenc} , decreases with noise but is consistently better than the encoded state fidelity F_{enc} even after applying Π_A , as indicated by F_A . A drastic improvement in fidelity is observed for states projected using projector Π_P . Not only is this fidelity, F_P , higher than F_A , it outperforms F_{unenc} up to a noise value of $\sim 2\%$. Combining the two post-selection methods results in the best fidelity, F_{AP} , for this circuit

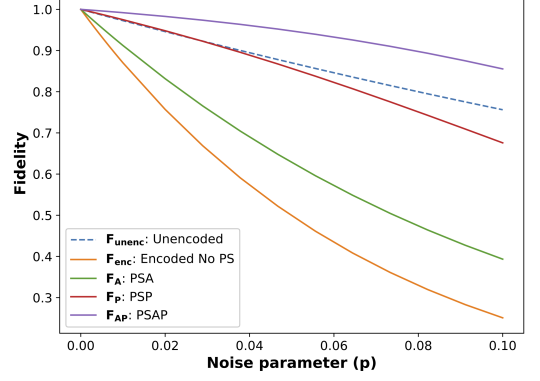


FIG. 10. Fidelity of the states prepared by numerically simulating the respective unencoded state, $[[4,2,2]]$ encoded state and projected states corresponding to the post-selection methods, PSA, PSP and PSAP, with increasing standard depolarizing noise, p .

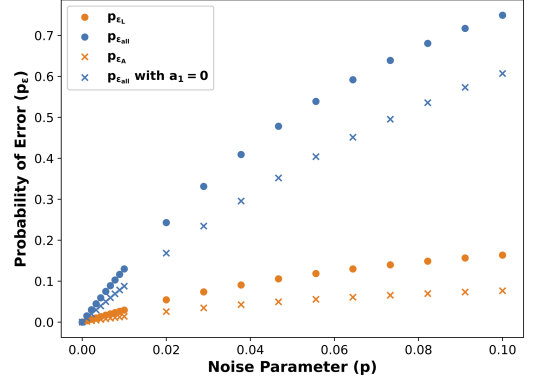


FIG. 11. Probability of Error, (p_e) in the encoded circuit with increasing two-qubit depolarizing noise. Plot labeled with $a_1 = 0$ are errors in the state projected with $a_1 = 0$

and is better than F_{unenc} for all noise parameters considered. Furthermore, overall decrease in fidelity of all cases with increasing noise in spite of projecting states against single- and multi-qubit errors is due to errors that go undetected in each projection, such as logical errors, introduced by the UCC ansatz or by combination of errors from state-preparation and UCC ansatz, that escaped detection by projection using Π_{AP} .

Both fidelity and accuracy of the energy estimates in the simulated encoded and unencoded circuits are im-

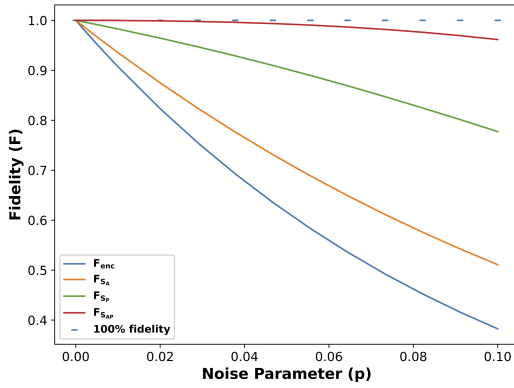


FIG. 12. State fidelity for the noisy logical input $|00\rangle$ state preparation and the projected states from the circuit labeled “STATE PREP” in Figure 3 and shown in Figure 6

ected by the errors introduced by the depolarizing error model. In the encoded circuit, in particular, the single- and two-qubit gate errors in the noise model manifest as logical, p_{ϵ_L} or non-logical errors ($p_{\epsilon_{NL}}$) in the final noisy mixed state. We present the probability of logical errors, p_{ϵ_L} , in the encoded circuit and in the projected state with $a_1 = 0$ (p_{ϵ_A}) in Figure 11 and also present the probability of all errors with increasing two-qubit depolarizing noise. While the errors increase with increasing noise, the proportion of all errors that are logical is much smaller. Since a logical error in this encoding requires an error event on a minimum of two qubits, the small proportion of logical errors indicate that a large proportion of errors in the encoded circuit are non-logical, single- and multi-qubit errors. Both $p_{\epsilon_{all}}$ and p_{ϵ_A} for states projected with $a_1 = 0$ are lower than the original state.

We also present the fidelity with increasing two-qubit depolarizing noise p for the encoded input state $|00\rangle$ and the states projected using S_A , S_P and S_{AP} in Figure 12 to better understand the contribution of a_1 to the improvement in the accuracy of the energy estimate. We compare the fidelity of the state projected by S_P with S_{AP} for the same final encoded input state $|00\rangle$. Improvement in fidelity, F_{S_P} , is due to the removal of states with single qubit bit-flip errors by projection operator S_P . Combining the methods using projector S_{AP} not only improves the fidelity over the fidelity F_{S_P} for the state projected by S_P , but also results in fidelity that is nearly 1 at $\lesssim 5\%$ noise.

B. Accuracy under a Realistic Noise Model

We present results from noisy simulations on the Quantinuum H1-1E emulator with their default error model. Their default error model closely mimics their H1-1 device. We present energy estimates and the corresponding SEM for molecular hydrogen with the unencoded ansatz and the encoded ansatz with and without post-selection. For results with post-selection, we also

show the POS. We additionally present these results with the encoding for RED for both the unencoded and encoded ansatzes with the corresponding the probability of success. We describe the reference names used for the different simulations presented in this section in Table III.

We first present results of the energy estimates of simulation of the unencoded ansatz and the encoded ansatz with post-selection with and without RED in Table IV. The table includes the energy estimates with and without RED of the unencoded ansatz and the best post-selection method of the encoded ansatz, PSAP, along with the corresponding difference, ΔE , from the exact energy of -1.13712Ha and the probability of success, η . When estimating energy of the the $[[4,2,2]]$ -encoded ansatz with the $[3,1]$ -RED at three parameter values $\theta \in [-0.400606, -0.22967, -0.058734]$, θ^* was found to correspond with the value calculated analytically at -0.22967 rads.

We now show results of the energy estimates of simulations without and with RED of the unencoded ansatz, and the encoded ansatz with post-selection in Figure 13. This figure additionally has the corresponding noiseless estimates from the emulator as a reference. The shaded gray area represents the region within chemical accuracy or ± 1.6 mHa of the exact energy for molecular hydrogen at 0.74\AA . Error bars indicate the standard error of the mean. In this simulation, without RED, the unencoded ansatz results in the lowest energy estimate compared to the best and lowest energy estimates from encoded ansatz, i.e., with the PSAP strategy. Neither estimate, however, reaches chemical accuracy.

Employing RED leads to dramatic decrease in energy estimates for the encoded ansatz, quantitatively presented in Table IV. For the unencoded ansatz, the code only results in a slight decrease in the energy compared to the results without RED. The magnitude of reduction in the energy estimate for all post-selection methods of the $[[4,2,2]]$ -encoded ansatz when using RED is greater than the corresponding decrease in energy for the unencoded ansatz. Comparing the energy estimates with RED for the unencoded and $[[4,2,2]]$ -encoded ansatz shows that not only does RED significantly improve the energy estimate for the $[[4,2,2]]$ -encoded ansatz, the best estimate, the PSAP method, with the $[3,1]$ -RED is about 1.37 mHa from the exact energy as shown in Table IV and within chemical accuracy. The second best estimate, from the PSP method, is also lower than that of the unencoded ansatz. In the case of the unencoded ansatz with RED the estimates are above the chemical accuracy regime with the energy difference from the exact energy being ~ 3.17 mHa, which is about ~ 1.6 mHa higher than chemical accuracy. The difference in the best estimate between the unencoded and $[[4,2,2]]$ -encoded ansatz is about 1.8 mHa.

We present the probability of success for the encoded ansatz simulation in Figure 14 with and without RED. There is a drop in probability of success of $\sim 2\%$ for the

TABLE III. Index of reference names used for different simulations with their descriptions.

Simulation Reference	Description
Unenc/Enc noiseless	Noiseless simulation of the unencoded/encoded ansatz on the Quantinuum H1-1 emulator.
Unencoded	Simulation of unencoded ansatz with default error model of the Quantinuum H1-1 emulator.
Unenc [3,1]-RED	Simulation of unencoded ansatz with [3,1]-RED encoding with default error model of the Quantinuum H1-1 emulator.
Enc PSA/PSP/PSAP/no PS	Simulation of [[4,2,2]]-encoded ansatz with default error model of the Quantinuum H1-1 emulator with PSA, PSP, PSAP or without PS.
Enc [3,1]-RED PSA/PSP/PSAP/no PS	Simulation of [[4,2,2]]-encoded ansatz with [3,1]-RED encoding on the Quantinuum H1-1 emulator with default error model with PSA, PSP, PSAP or without PS.

TABLE IV. Energy and Probability of Success (η) with and without RED for unencoded and [[4,2,2]]-Encoded ansatz with post-selection methods.

Simulation	Energy (mHa)	ΔE (mHa)	η (%)
Unencoded	-1133.39 ± 0.51	3.73	100
Encoded PSAP	-1129.78 ± 0.75	7.33	49.2
Unencoded with [3,1]-RED	-1133.94 ± 0.51	3.17	98.2
Encoded PSAP with [3,1]-RED	-1135.74 ± 0.73	1.37	47.3

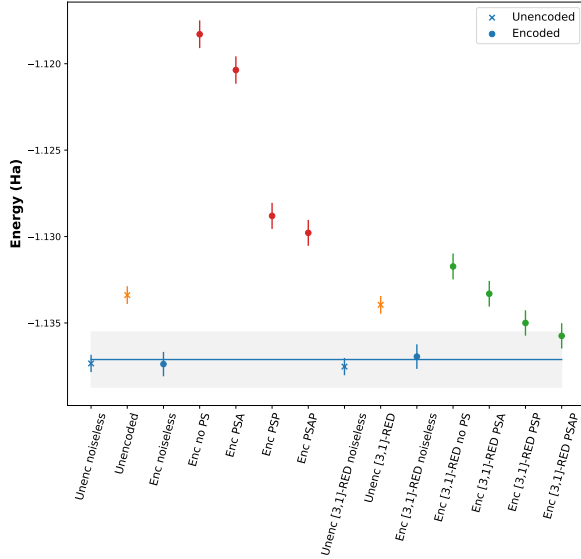


FIG. 13. Energy estimates of unencoded and [[4,2,2]]-encoded simulations with post-selection without and with [3,1]-RED on the Quantinuum H1-1E emulator with the default error model. Shaded grey area represents the chemical accuracy region.

post-selection methods with [3,1]-RED from the simulations without RED but the corresponding drop in energy for the method with the best estimate, the PSAP method, with [3,1]-RED is nearly 6 mHa. The corresponding difference in energy for the best estimate with the unencoded ansatz is 0.6 mHa for a loss of 1.8% of sam-

ples as shown in Table IV. Additionally, the probability of success in the case of the unencoded ansatz is from 100% and for the [[4,2,2]]-encoded ansatz, from $\sim 50\%$ as the implementation of gate teleportation with ancilla a_2 results in a uniform superposition of two equivalent states of which we only use one.

Finally, we present the resources required for the simulations of the [[4,2,2]]-encoded and unencoded ansatz for the best energy estimate with [3,1]-RED in Table V based on the simulations on the emulator. Shots or number of samples are displayed as twice the amount since two circuit executions are required, one each for measuring the Z_0Z_1 and X_0X_1 Pauli term. Per run indicates the number of said resource that is required per execution of the circuit including parallel circuits. Parallel circuits per run are 0 for the encoded ansatz with [3,1]-RED as only one 18-qubit circuit can be executed on the 20-qubit emulator at a time, whereas three unencoded circuits can be executed with [3,1]-RED. Maximum number of single qubit gates point to the circuit for measuring “ X_0X_1 ” Pauli term, which requires execution of additional Hadamard gates. Both the total number of qubits required for parallel executions and number of qubits required per ansatz execution is presented.

The expected cost is an approximate estimate of the total cost required as calculated by the Quantinuum emulator for executing these simulations on the Quantinuum device. Although this is not typically included in resource estimates, as devices become available for users commercially, there is a corresponding charge for accessing the devices which imposes an additional constraint that must be considered when evaluating the cost of

TABLE V. Resource analysis for estimating the ground state energy within chemical accuracy on the Quantinuum H1-1E emulator with $[[3,1]]$ -RED for the unencoded and $[[4,2,2]]$ -encoded ansatzes.

Resources	Unencoded	$[[4,2,2]]$ -Encoded
Shots	2×62700	2×188000
Parallel Circuits per Run	3	0
Number of qubits per Ansatz with $[[3,1]]$ -RED	6	18
Number of qubits per Run with $[[3,1]]$ -RED	18	18
Max. Single-qubit Gates per Run	9	7
Two-qubit Gates per Run	18	25
Measurements per Run	18	18
Estimated Total Runtime	8.5 hrs	1.5 days
Expected cost of credits	10200	31400

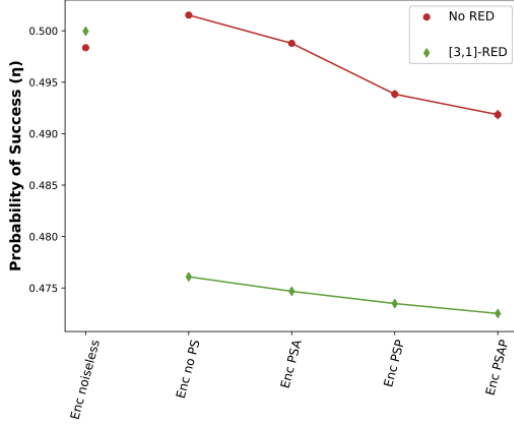


FIG. 14. Probability of Success for Encoded Simulations on the Quantinuum H1-1E emulator with and without RED.

implementing such benchmarks on commercial devices, such as, Quantinuum. The cost of credits is calculated by the emulator using the formula shown in Equation 19 and is provided by Quantinuum in their product data sheet.

$$HQC = 5 + \frac{N_{1q} + 10N_{2q} + 5N_m}{5000}C \quad (19)$$

where N_{1q} , N_{2q} and N_m are number of native single-qubit gates, two-qubit gates and state preparation and measurement operations in the circuit, respectively and C is the number of shots. The product data sheet also suggests that the estimated run time for circuits is about an hour for circuits that require between 500 to 1200 HQCs, which depends on different factors such as the number of the connectivity required for the circuit and the dynamic calibrations of the system. The estimated total runtime in Table V have been calculated by assuming execution of circuits worth 1200 credits per hour for the simple unencoded ansatz and about 800 credits per hour, the average of the two extremes of 500 and 1200, for the slightly more complicated encoded circuit.

VI. DISCUSSION

The results indicate that using error detection for mitigating the dominant sources of error can enable the estimates to reach the targeted level of accuracy and precision, which, in this case, is chemical accuracy. Simulations with only the depolarizing error channel indicate that the $[[4,2,2]]$ QED code improves energy estimates over the unencoded ansatz when using post-selection by logical state parity, PSP, by itself at low noise values, and in combination with post-selection by ancilla, a_1 , measurement, PSAP, at least up to 10% noise. The latter also results in energy estimates within chemical accuracy at the highest noise threshold of all the simulations.

The decrease in precision of the estimated energy calculated from post-selected results of the simulation of the encoded ansatz compared to the unencoded ansatz is due to consideration of only one half of the results from the use of gate teleportation. This is particularly remarkable when considering that the number of samples used to calculate the energy estimate is nearly half as many as that used for the unencoded ansatz but results in only ~ 0.2 mHa increase in standard error with a significant improvement in accuracy. Within the different post-selection methods, improvement in precision is consistent with improvement in logical fidelity, indicating that in addition to improvement in the accuracy of the energy estimate, post-selection also improves the corresponding precision of the calculation. The improvement in precision in spite of increasing loss of samples with increasing accuracy of the post-selection method is a result of the improvement in variance of the calculation. We see similar improvement in precision for the encoded ansatz when using the RED code under the Quantinuum H1-1E error model.

Simulations under the device error model without RED indicate that the unencoded energy estimate results in a lower energy than the best post-selection strategy for the $[[4,2,2]]$ -encoded ansatz, the PSAP energy estimate. Both ansatzes result in lower energies with RED. Using RED in addition to the PSAP method of the $[[4,2,2]]$ -encoded ansatz results in an estimate of energy that is nearly 1.8 mHa lower than the best unencoded energy estimate and within chemical accuracy. Numerical simu-

lations of the $[[4,2,2]]$ -encoded ansatz under an isotropic two-qubit depolarizing error model without any readout error indicated that the threshold at which the energy estimate reached chemical accuracy was 0.09% as shown in Figure 7. The Quantinuum emulator error model not only includes read-out error but also models depolarizing error with an asymmetric channel and includes leakage by spontaneous emission as part of the depolarizing error model. The energy estimate reaching chemical accuracy with the $[3,1]$ -RED suggests that the readout error was nearly completely eliminated and that the $[[4,2,2]]$ -encoding is at least as effective at detecting errors with this depolarizing error model as with the isotropic error model. Additionally, even though the other error sources listed in Table I are an order(s) of magnitude lower than the leading error sources, they were not considered in the numerical simulations with the isotropic depolarizing error model and yet resulted in a similar estimate indicating that they did not have as much of an effect on decreasing the accuracy.

The deviation of the estimated energy using the PSP and PSAP methods from the corresponding energy expectation value calculation using the density matrix, occurs due to the difference in order of operations between the two methods. In the latter, the states of interest are projected and the expectation value is calculated from these states. In the former, the bitstrings are post-selected from the measurement of the final state and then the expectation values are calculated from these post-selected bitstrings. Post-selection strategies using a_1 lead to improvement in accuracy of the energy estimate due to detection of single and multi-qubit error events. Nearly unity fidelity for projecting states with logical state parity and $a_1 = 0$ measurement (F_{SAP}) indicates that a_1 detects nearly all multi-qubit error events that are left undetected by projecting states with logical state parity alone. Additionally, the reduction in probability of logical errors in the state projected for $a_1 = 0$ measurement, further confirm the detection of errors other than single qubit errors by a_1 .

As an application benchmark, the study demonstrates that effectively removing errors in every sample measurement using methods such as QED and readout error detection can sufficiently manage dominant sources of errors typically found in current commercial devices and lead to the targeted accuracy if the error rate is sufficiently low. However, as can be seen from the resource analysis, the benchmark with error detection leads to a large increase in resource overhead with a three-fold increase in the number of qubits and two-qubit gates alone compared to the unencoded ansatz, not to mention the corresponding increase in the cost to use the device. Such an increase in resources suggests that scaling up the benchmark exactly as it is to systems of larger scale may be prohibitive.

Resource scaling depends both on the choice of ansatz and the quantum error detection or correction scheme. The analysis is presented for the smallest molecular sys-

tem using the smallest error detection code for a device with all-to-all connectivity, making it the best case scenario in terms of resources required. Increase in size of the molecular system, constraints in device connectivity, and change in quantum error correction/detection code will inevitably lead to an increase in the resources required. While the study demonstrates that the methods lead to an effective benchmark, in order for such benchmarks to be applicable for more useful larger scale systems across device architectures innovative methods to optimize the scaling of resources with increase in system size are needed especially as technologies grow and error rates become lower. In this study itself, implementation of the rotation gate in the $[[4,2,2]]$ -encoded ansatz without the consequence of losing nearly half the samples in the process would have led to a decrease in at least one of the resources: number of samples or shots compared to the unencoded ansatz. Similarly, optimizing ansatzes, using flag qubits to reduce overhead of larger QEC codes, and combining other error mitigation techniques may be potential avenues for future work to improve the resource overhead of the benchmark presented here with increase in system size.

VII. CONCLUSION

We have demonstrated that error detection codes with post-selection lead to an energy estimate within chemical accuracy for a small two-electron system. We have presented results from noisy simulations of the ground state of molecular hydrogen using VQE under the depolarizing error model and the error model of a commercial quantum computing device, Quantinuum H1-1. The aim was to assess the impact of different post-selection methods on the energy accuracy and evaluate the outcomes against the benchmark of chemical accuracy, defined as the estimated energy being within 1.6 mHa of the exact energy, by using the $[[4,2,2]]$ QED code and RED with post-selection to mitigate gate depolarizing error and readout error, respectively. We found that the results demonstrate the improvement in the accuracy and precision of energy estimates with the best estimate reaching chemical accuracy indicating effective mitigation of both gate and readout error. The two-qubit gate error rate of the emulator at 0.088% is slightly lower than the threshold, assessed by numerical simulations with the depolarizing error model, at which the $[[4,2,2]]$ -encoded ansatz resulted in an energy estimate within chemical accuracy for molecular hydrogen. This indicates that the readout error was sufficiently removed with the $[3,1]$ -RED code, which was the only method to result in energy estimates within chemical accuracy.

Using $[[4,2,2]]$ -QED with post-selection based on detection of single qubit errors alone improves the accuracy of the energy estimate at low noise levels. Combining this post-selection method with post-selection using an ancilla for single and multi-qubit error detection during

input state preparation further improves the accuracy of the estimate at noise levels as high as 10%. Constructing the input state-preparation circuit such that the control qubit for all the two-qubit $CNOT$ gates is q_0 , which is entangled with a_1 makes the detection of multi-qubit errors possible.

Our framework for benchmarking is an investigation of accuracy of a small quantum application on a quantum device. As described earlier, computational accuracy of a device is characterized both by the difference in magnitude of estimated outcome from the exact outcome and the precision of the estimate. The latter is an indication of how reproducible the accuracy is on the given device. Error mitigation techniques typically are applied to the estimated average and the improvement in the accuracy often leads to an increase in variance [50]. This framework improves both accuracy and precision by removing detected errors from every measured sample prior to calculating the average. Using additional error detection for combating readout error maintains this structure and similarly improves accuracy without decreasing the precision of the estimate. The scaling of resources with system size is the main limiting factor of this benchmark and we defer studies to improve this scaling to future work.

ACKNOWLEDGMENTS

This work was supported the U.S. Department of Energy Advanced Scientific Computing Research program office under the Accelerated Research for Quantum Computing program. This research used resources of the Oak Ridge Leadership Computing Facility at the Oak Ridge National Laboratory, which is supported by the Office of Science of the U.S. Department of Energy under Contract No. DE-AC05-00OR22725. D.C. acknowledges the support from the “Embedding Quantum Computing into Many-body Frameworks for Strongly Correlated Molecular and Materials Systems” project, which is funded by the U.S. Department of Energy (DOE), the Office of Science, the Office of Basic Energy Sciences, and the Division of Chemical Sciences, Geosciences, and Biosciences.

Appendix A: Hamiltonian encoding

We start with the exact electronic Hamiltonian for molecular hydrogen in second quantized form:

$$\begin{aligned}
 H(R) = & h_{00}a_0^\dagger a_0 + h_{22}a_2^\dagger a_2 + h_{33}a_3^\dagger a_3 + h_{11}a_1^\dagger a_1 \\
 & + h_{2002}a_2^\dagger a_0^\dagger a_0 a_2 + h_{3113}a_3^\dagger a_1^\dagger a_1 a_3 + h_{2112}a_2^\dagger a_1^\dagger a_1 a_2 \\
 & + h_{0330}a_0^\dagger a_3^\dagger a_3 a_0 + (h_{2332} - h_{2323})a_2^\dagger a_3^\dagger a_3 a_2 \\
 & + (h_{0110} - h_{0101})a_0^\dagger a_1^\dagger a_1 a_0 \\
 & + h_{2103}(a_2^\dagger a_1^\dagger a_0 a_3 + a_3^\dagger a_0^\dagger a_1 a_2) \\
 & + h_{2013}(a_2^\dagger a_0^\dagger a_1 a_3 + a_3^\dagger a_1^\dagger a_0 a_2)
 \end{aligned} \tag{A1}$$

TABLE VI. Mapping of fermionic basis to qubit basis for all possible states of the hydrogen molecule with the spin-singlet configuration. Indices for the fermionic basis correspond with indices in Equation A2 and indices for the qubit basis correspond with the qubits used in the circuit construction of the unitary operator.

$ \Psi_3\Psi_2\Psi_1\Psi_0\rangle$	$ q_0q_1\rangle$
$ 0101\rangle$	$ 00\rangle$
$ 0110\rangle$	$ 01\rangle$
$ 1001\rangle$	$ 10\rangle$
$ 1010\rangle$	$ 11\rangle$

The molecular orbitals $|\psi_u\rangle$ and $|\psi_g\rangle$ are given as linear combinations of the respective atomic orbitals, leading to spin orbitals $|\Psi_i\rangle$ each with spin \uparrow or \downarrow [40, 51], as

$$|\psi_g\rangle = |\psi_1\rangle + |\psi_2\rangle \tag{A2a}$$

$$|\psi_u\rangle = |\psi_1\rangle - |\psi_2\rangle \tag{A2b}$$

$$|\Psi_0\rangle = |\psi_g(\uparrow)\rangle \tag{A3a}$$

$$|\Psi_1\rangle = |\psi_u(\uparrow)\rangle \tag{A3b}$$

$$|\Psi_2\rangle = |\psi_g(\downarrow)\rangle \tag{A3c}$$

$$|\Psi_3\rangle = |\psi_u(\downarrow)\rangle \tag{A3d}$$

The possible states within the spin-singlet configuration in the fermionic basis for the hydrogen molecule and the corresponding states in the two qubit basis are presented in Table VI. The indices correspond with those of the molecular orbitals in Equation A2.

We define the qubit excitation, de-excitation and number operators as in [51]

$$\begin{aligned}
 Q^+ &= |1\rangle\langle 0| = \frac{1}{2}(X - iY) \\
 Q^- &= |0\rangle\langle 1| = \frac{1}{2}(X + iY) \\
 N^{(0)} &= |0\rangle\langle 0| = \frac{1}{2}(I + Z) \\
 N^{(1)} &= |1\rangle\langle 1| = \frac{1}{2}(I - Z)
 \end{aligned} \tag{A4}$$

where X , Y , and Z are the Pauli operators. These operators are used to construct the reduced two-qubit Hamiltonian by using the mapping presented in Table VII.

The electronic Hamiltonian is then reduced as

$$H = \sum_{pq} h_{pq} E_{pq} + \frac{1}{2} \sum_{pqrs} h_{pqrs} \delta_{qr} E_{ps} - E_{pr} E_{qs} \tag{A5}$$

where $E_{pq} = a_p^\dagger a_q$ includes terms with $p = q$ and are presented in Table VII. Using these operators we proceed to transform the electronic Hamiltonian in Equation A1

TABLE VII. Fermionic (de)excitation and number operators mapped to the corresponding qubit and Pauli operators, where E_{pq} represents the excitation and number operators when $p \neq q$ and $p = q$, respectively. The Pauli operators are constructed using Equation A4.

Operator	Fermionic operators	Qubit operators	Pauli operators for qubits
E_{10}	$ 0110\rangle\langle 0101 + 1010\rangle\langle 1001 $	$ 01\rangle\langle 00 + 11\rangle\langle 10 $	$\frac{1}{2}(X_0 - iY_0)$
E_{32}	$ 1001\rangle\langle 0101 + 1010\rangle\langle 0110 $	$ 10\rangle\langle 00 + 11\rangle\langle 01 $	$\frac{1}{2}(X_1 - iY_1)$
E_{00}	$ 0101\rangle\langle 0101 + 1001\rangle\langle 1001 $	$ 00\rangle\langle 00 + 10\rangle\langle 10 $	$\frac{1}{2}(I + Z_0)$
E_{11}	$ 0110\rangle\langle 0110 + 1010\rangle\langle 1010 $	$ 01\rangle\langle 01 + 11\rangle\langle 11 $	$\frac{1}{2}(I - Z_0)$
E_{22}	$ 0101\rangle\langle 0101 + 0110\rangle\langle 0110 $	$ 00\rangle\langle 00 + 01\rangle\langle 01 $	$\frac{1}{2}(I + Z_1)$
E_{33}	$ 1001\rangle\langle 1001 + 1010\rangle\langle 1010 $	$ 10\rangle\langle 10 + 11\rangle\langle 11 $	$\frac{1}{2}(I - Z_1)$

to a qubit representation:

$$\begin{aligned}
H = & (h_{00} + h_{33} + \frac{1}{4}(h_{2002} + h_{3113} + h_{2112} + h_{0330}))I \\
& + (h_{00} - h_{11} + \frac{1}{4}(h_{2002} - h_{3113} - h_{2112} + h_{0330}))Z_0 \\
& + (h_{22} - h_{33} + \frac{1}{4}(h_{2002} - h_{3113} + h_{2112} - h_{0330}))Z_1 \\
& + \frac{1}{4}(h_{2002} + h_{3113} - h_{2112} - h_{0330})Z_1Z_0 + 0 + 0 \\
& + h_{2103}(\frac{1}{2}(-X_1X_0 - Y_1Y_0)) \\
& + h_{2013}(\frac{1}{2}(-X_1X_0 + Y_1Y_0))
\end{aligned} \tag{A6}$$

$$\begin{aligned}
g_0 = & h_{00} + h_{33} + \frac{1}{4}(h_{2002} + h_{3113} + h_{2112} + h_{0330}) \\
g_1 = & h_{00} - h_{11} + \frac{1}{4}(h_{2002} - h_{3113} - h_{2112} + h_{0330}) \\
g_2 = & h_{22} - h_{33} + \frac{1}{4}(h_{2002} - h_{3113} + h_{2112} - h_{0330}) \\
g_3 = & \frac{1}{4}(h_{2002} + h_{3113} - h_{2112} - h_{0330}) \\
g_4 = & -h_{2103}
\end{aligned} \tag{A7}$$

Additionally:

$$\begin{aligned}
g_1 &= g_2 \\
h_{2013} &= h_{2103} \\
h_{2112} &= h_{0330}
\end{aligned} \tag{A8}$$

This leads to the final two-qubit Hamiltonian shown in Equation 3.

Appendix B: Unitary operator

The unitary operator approximated to the first Trotter step is shown in Equation B1 [52].

$$\begin{aligned}
U(\theta) &= e^{T(\theta) - T(\theta)^\dagger} = e^{\sum_i \theta_i (\tau_i - \tau_i^\dagger)} \\
&\approx \left(\prod_i e^{\frac{\theta_i}{t} (\tau_i - \tau_i^\dagger)} \right)^t \\
&\approx \prod_i e^{\theta_i (\tau_i - \tau_i^\dagger)}
\end{aligned} \tag{B1}$$

$$\begin{aligned}
T(\theta) &= \sum_k T_k(\theta) \\
T_1 &= \sum_{q \in occ, p \in virt} \theta_q^p a_p^\dagger a_q \\
T_2 &= \sum_{r > s \in occ, p > q \in virt} \theta_{rs}^{pq} a_p^\dagger a_q^\dagger a_r a_s
\end{aligned} \tag{B2}$$

where T_k is the excitation operator manifold and θ_q^p and θ_{rs}^{pq} are singles and doubles amplitudes, respectively and p, q and r, s are virtual or unoccupied and occupied orbitals, respectively. To transform the fermionic unitary operator to a qubit representation specific to our encoding we use qubit operators from Equation A4. Considering only the doubles contribution in Equation B1 and Equation B2, we replace the fermionic operators in T_2 with qubit operators using Equation A4 as shown in Equation B3.

$$\begin{aligned}
T_2 &= \sum_{p > q \in occ, r > s \in virt} \theta_{rs}^{pq} (a_p^\dagger a_q^\dagger a_r a_s - a_s a_r a_q^\dagger a_p^\dagger) \\
&= \theta_{31}^{20} (a_2^\dagger a_0^\dagger a_3 a_1 - a_1^\dagger a_3^\dagger a_0 a_2) \\
&= \theta_{31}^{20} (E_{10} E_{32} - E_{23} E_{01}) \\
&= i\theta_{31}^{20} \frac{1}{2} (-Y_0 X_1 - Y_0 X_1 Z_0 Z_1)
\end{aligned} \tag{B3}$$

where we have used $Y_k Z_k = iX_k$, $X_k Z_k = -iY_k$, to factorize the operator in the final step. Considering our reference state $|00\rangle$, we arrive at the reduced UCC doubles ansatz as shown in Equation B4:

$$\begin{aligned}
U(\theta) &= e^{i\frac{\theta}{2}(-Y_0 X_1)} e^{i\frac{\theta}{2}(-Y_0 X_1 Z_0 Z_1)} \\
&= e^{i\frac{\theta}{2}(-Y_0 X_1)} e^{i\frac{\theta}{2}(-Y_0 X_1)} \\
&= e^{-i\theta Y_0 X_1}
\end{aligned} \tag{B4}$$

TABLE VIII. Basis operations.

Basis Operations	
Logical Basis	Physical Basis
$X_1 \otimes I_2$	$X \otimes I \otimes X \otimes I$
$I_1 \otimes X_2$	$X \otimes X \otimes I \otimes I$
$Z_1 \otimes I_2$	$Z \otimes Z \otimes I \otimes I$
$I_1 \otimes Z_2$	$Z \otimes I \otimes Z \otimes I$
$H_1 \otimes H_2$	$H \otimes H \otimes H \otimes H$
$CNOT_{12}$	$SWAP_{12}$
$CNOT_{21}$	$SWAP_{13}$

Appendix C: Basis states and operations for the $[[4,2,2]]$ code

The basis states for the logical codespace of this encoding are shown in Equation C1 and the corresponding physical operations for each logical operation are described in Table VIII.

$$\begin{aligned}
|\overline{00}\rangle &= \frac{1}{\sqrt{2}}(|0000\rangle + |1111\rangle) \\
|\overline{10}\rangle &= \frac{1}{\sqrt{2}}(|0101\rangle + |1010\rangle) \\
|\overline{01}\rangle &= \frac{1}{\sqrt{2}}(|0011\rangle + |1100\rangle) \\
|\overline{11}\rangle &= \frac{1}{\sqrt{2}}(|0110\rangle + |1001\rangle)
\end{aligned} \tag{C1}$$

Appendix D: Projection operators for $[[4,2,2]]$ -encoded VQE ansatz

We use the following projection operators to calculate the logical fidelity of the states corresponding to each post-selection strategy of the $[[4,2,2]]$ -encoded VQE

ansatz.

$$\Pi_A = |0\rangle\langle 0|_{a_1} \otimes |\mathbb{I}_0\mathbb{I}_1\mathbb{I}_2\mathbb{I}_3\rangle\langle \mathbb{I}_0\mathbb{I}_1\mathbb{I}_2\mathbb{I}_3| \otimes |0\rangle\langle 0|_{a_2=0} \tag{D1a}$$

$$\begin{aligned}
\Pi_P &= \mathbb{I}_{a_1} \otimes (|\overline{00}\rangle\langle \overline{00}|_{q_0-q_3} + |\overline{01}\rangle\langle \overline{01}|_{q_0-q_3} \\
&\quad + |\overline{10}\rangle\langle \overline{10}|_{q_0-q_3} + |\overline{11}\rangle\langle \overline{11}|_{q_0-q_3}) \otimes |0\rangle\langle 0|_{a_2=0}
\end{aligned} \tag{D1b}$$

$$\Pi_{AP} = \Pi_A \otimes \Pi_P \tag{D1c}$$

Appendix E: Projection operators for $[[4,2,2]]$ -encoded input state

We calculate the fidelity corresponding to each post-selection method for the $[[4,2,2]]$ -encoded input state $|\overline{00}\rangle$ by projecting states (i) with $a_1 = |0\rangle$, (ii) within the codespace, and (iii) both within the codespace and with $a_1 = |0\rangle$, using projection operators, S_A , S_P , and S_{AP} , respectively. We use Equation 13 to calculate the fidelity, F_{S_i} , of the projected states where, in this case, $\rho_1 = |\phi\rangle\langle \phi|$ is the noiseless encoded state, $\rho_i = \frac{S_i \rho_{noisy} S_i^\dagger}{\text{Tr}(S_i \rho_{noisy} S_i^\dagger)}$ for $S_i \in \{S_A, S_P, S_{AP}\}$ are the projected states and ρ_{noisy} is the noisy encoded input state.

$$\begin{aligned}
|\phi\rangle &= |a_1\rangle \otimes |\overline{00}\rangle \\
&= |0\rangle \otimes \frac{1}{\sqrt{2}}(|0000\rangle + |1111\rangle)
\end{aligned} \tag{E1}$$

$$S_A = |0\rangle\langle 0|_{a_1} \otimes |\mathbb{I}_0\mathbb{I}_1\mathbb{I}_2\mathbb{I}_3\rangle\langle \mathbb{I}_0\mathbb{I}_1\mathbb{I}_2\mathbb{I}_3| \tag{E2a}$$

$$\begin{aligned}
S_P &= \mathbb{I}_{a_1} \otimes (|\overline{00}\rangle\langle \overline{00}|_{q_0-q_3} + |\overline{01}\rangle\langle \overline{01}|_{q_0-q_3} \\
&\quad + |\overline{10}\rangle\langle \overline{10}|_{q_0-q_3} + |\overline{11}\rangle\langle \overline{11}|_{q_0-q_3})
\end{aligned} \tag{E2b}$$

$$S_{AP} = S_A \otimes S_P \tag{E2c}$$

-
- [1] G. Q. AI, Suppressing quantum errors by scaling a surface code logical qubit, *Nature* **614**, 676 (2023).
 - [2] S. J. Evered, D. Bluvstein, M. Kalinowski, S. Ebadi, T. Manovitz, H. Zhou, S. H. Li, A. A. Geim, T. T. Wang, N. Maskara, *et al.*, High-fidelity parallel entangling gates on a neutral atom quantum computer, arXiv preprint arXiv:2304.05420 (2023).
 - [3] K. Yamamoto, S. Duffield, Y. Kikuchi, and D. M. Ramo, Demonstrating bayesian quantum phase estimation with quantum error detection, *Physical Review Research* **6**, 013221 (2024).
 - [4] P. Shor, Fault-tolerant quantum computation, in *Proceedings of 37th Conference on Foundations of Computer Science* (1996) pp. 56–65.
 - [5] P. W. Shor, Scheme for reducing decoherence in quantum computer memory, *Physical review A* **52**, R2493 (1995).
 - [6] A. M. Steane, Error correcting codes in quantum theory, *Physical Review Letters* **77**, 793 (1996).
 - [7] A. R. Calderbank and P. W. Shor, Good quantum error-correcting codes exist, *Physical Review A* **54**, 1098 (1996).
 - [8] S. J. Devitt, W. J. Munro, and K. Nemoto, Quantum error correction for beginners, *Reports on Progress in Physics* **76**, 076001 (2013).
 - [9] A. G. Fowler, M. Mariantoni, J. M. Martinis, and A. N. Cleland, Surface codes: Towards practical large-scale quantum computation, *Phys. Rev. A* **86**, 032324 (2012).
 - [10] S. Bravyi, A. W. Cross, J. M. Gambetta, D. Maslov, P. Rall, and T. J. Yoder, High-threshold and low-overhead fault-tolerant quantum memory (2024), arXiv:2308.07915 [quant-ph].

- [11] W. P. Livingston, M. S. Blok, E. Flurin, J. Dressel, A. N. Jordan, and I. Siddiqi, Experimental demonstration of continuous quantum error correction, *Nature communications* **13**, 2307 (2022).
- [12] V. Sivak, A. Eickbusch, B. Royer, S. Singh, I. Tsioutsios, S. Ganjam, A. Miano, B. Brock, A. Ding, L. Frunzio, *et al.*, Real-time quantum error correction beyond break-even, *Nature* **616**, 50 (2023).
- [13] C. Ryan-Anderson, J. G. Bohnet, K. Lee, D. Gresh, A. Hankin, J. Gaebler, D. Francois, A. Chernoguzov, D. Lucchetti, N. C. Brown, *et al.*, Realization of real-time fault-tolerant quantum error correction, *Physical Review X* **11**, 041058 (2021).
- [14] S. Krinner, N. Lacroix, A. Remm, A. Di Paolo, E. Genois, C. Leroux, C. Hellings, S. Lazar, F. Swiadek, J. Herrmann, *et al.*, Realizing repeated quantum error correction in a distance-three surface code, *Nature* **605**, 669 (2022).
- [15] R. Acharya, I. Aleiner, R. Allen, T. I. Andersen, M. Ansmann, F. Arute, K. Arya, A. Asfaw, J. Atalaya, R. Babush, D. Bacon, J. C. Bardin, J. Basso, A. Bengtsson, S. Boixo, G. Bortoli, A. Bourassa, J. Bovaird, L. Brill, M. Broughton, B. B. Buckley, D. A. Buell, T. Burger, B. Burkett, N. Bushnell, Y. Chen, Z. Chen, B. Chiaro, J. Cogan, R. Collins, P. Conner, W. Courtney, A. L. Crook, B. Curtin, D. M. Debroy, A. Del Toro Barba, S. Demura, A. Dunsworth, D. Eppens, C. Erickson, L. Faoro, E. Farhi, R. Fatemi, L. Flores Burgos, E. Forati, A. G. Fowler, B. Foxen, W. Giang, C. Gidney, D. Gilboa, M. Giustina, A. Grajales Dau, J. A. Gross, S. Habegger, M. C. Hamilton, M. P. Harrigan, S. D. Harrington, O. Higgott, J. Hilton, M. Hoffmann, S. Hong, T. Huang, A. Huff, W. J. Huggins, L. B. Ioffe, S. V. Isakov, J. Iveland, E. Jeffrey, Z. Jiang, C. Jones, P. Juhas, D. Kafri, K. Kechedzhi, J. Kelly, T. Khatkar, M. Khezri, M. Kieferová, S. Kim, A. Kitaev, P. V. Klimov, A. R. Klots, A. N. Korotkov, F. Kostritsa, J. M. Kreikebaum, D. Landhuis, P. Laptev, K.-M. Lau, L. Laws, J. Lee, K. Lee, B. J. Lester, A. Lill, W. Liu, A. Locharla, E. Lucero, F. D. Malone, J. Marshall, O. Martin, J. R. McClean, T. McCourt, M. McEwen, A. Megrant, B. Meurer Costa, X. Mi, K. C. Miao, M. Mohseni, S. Montazeri, A. Morvan, E. Mount, W. Mruczkiewicz, O. Naaman, M. Neeley, C. Neill, A. Nersisyan, H. Neven, M. Newman, J. H. Ng, A. Nguyen, M. Nguyen, M. Y. Niu, T. E. O'Brien, A. Opremcak, J. Platt, A. Petukhov, R. Potter, L. P. Pryadko, C. Quintana, P. Roushan, N. C. Rubin, N. Saei, D. Sank, K. Sankaragomathi, K. J. Satzinger, H. F. Schurkus, C. Schuster, M. J. Shearn, A. Shorter, V. Shvarts, J. Skrzynny, V. Smelyanskiy, W. C. Smith, G. Sterling, D. Strain, M. Szalay, A. Torres, G. Vidal, B. Villalonga, C. Vollgraf Heidweiller, T. White, C. Xing, Z. J. Yao, P. Yeh, J. Yoo, G. Young, A. Zalcman, Y. Zhang, N. Zhu, and Google Quantum AI, Suppressing quantum errors by scaling a surface code logical qubit, *Nature* **614**, 676 (2023).
- [16] K. Mayer, C. Ryan-Anderson, N. Brown, E. Durso-Sabina, C. H. Baldwin, D. Hayes, J. M. Dreiling, C. Foltz, J. P. Gaebler, T. M. Gatterman, J. A. Gerber, K. Gilmore, D. Gresh, N. Hewitt, C. V. Horst, J. Johansen, T. Mengle, M. Mills, S. A. Moses, P. E. Siegfried, B. Neyenhuis, J. Pino, and R. Stutz, Benchmarking logical three-qubit quantum Fourier transform encoded in the Steane code on a trapped-ion quantum computer (2024), arXiv:2404.08616 [quant-ph].
- [17] D. W. Leung, M. A. Nielsen, I. L. Chuang, and Y. Yamamoto, Approximate quantum error correction can lead to better codes, *Physical Review A* **56**, 2567 (1997).
- [18] E. Knill, Fault-tolerant postselected quantum computation: Threshold analysis, arXiv preprint quant-ph/0404104 (2004).
- [19] E. Knill, Quantum computing with realistically noisy devices, *Nature* **434**, 39 (2005), number: 7029 Publisher: Nature Publishing Group.
- [20] B. W. Reichardt, Error-Detection-Based Quantum Fault-Tolerance Threshold, *Algorithmica* **55**, 517 (2009).
- [21] Y. P. Zhong, Z. L. Wang, J. M. Martinis, A. N. Cleland, A. N. Korotkov, and H. Wang, Reducing the impact of intrinsic dissipation in a superconducting circuit by quantum error detection, *Nature Communications* **5**, 3135 (2014), number: 1 Publisher: Nature Publishing Group.
- [22] A. D. Córcoles, E. Magesan, S. J. Srinivasan, A. W. Cross, M. Steffen, J. M. Gambetta, and J. M. Chow, Demonstration of a quantum error detection code using a square lattice of four superconducting qubits, *Nature communications* **6**, 6979 (2015).
- [23] D. Gottesman, Quantum fault tolerance in small experiments, arXiv preprint arXiv:1610.03507 (2016).
- [24] C. Vuillot, Is error detection helpful on ibm 5q chips?, arXiv preprint arXiv:1705.08957 (2017).
- [25] N. M. Linke, M. Gutierrez, K. A. Landsman, C. Figgatt, S. Debnath, K. R. Brown, and C. Monroe, Fault-tolerant quantum error detection, *Science advances* **3**, e1701074 (2017).
- [26] D. Willsch, M. Willsch, F. Jin, H. De Raedt, and K. Michielsen, Testing quantum fault tolerance on small systems, *Physical Review A* **98**, 052348 (2018).
- [27] M. Takita, A. W. Cross, A. Córcoles, J. M. Chow, and J. M. Gambetta, Experimental Demonstration of Fault-Tolerant State Preparation with Superconducting Qubits, *Physical Review Letters* **119**, 180501 (2017).
- [28] S. Rosenblum, P. Reinhold, M. Mirrahimi, L. Jiang, L. Frunzio, and R. J. Schoelkopf, Fault-tolerant detection of a quantum error, *Science* **361**, 266 (2018), publisher: American Association for the Advancement of Science.
- [29] J. Roffe, D. Headley, N. Chancellor, D. Horsman, and V. Kendon, Protecting quantum memories using coherent parity check codes, *Quantum Science and Technology* **3**, 035010 (2018).
- [30] E. H. Chen, T. J. Yoder, Y. Kim, N. Sundaresan, S. Srinivasan, M. Li, A. D. Córcoles, A. W. Cross, and M. Takita, Calibrated Decoders for Experimental Quantum Error Correction, *Physical Review Letters* **128**, 110504 (2022).
- [31] M. Urbanek, B. Nachman, and W. A. de Jong, Error detection on quantum computers improving the accuracy of chemical calculations, *Phys. Rev. A* **102**, 022427 (2020).
- [32] B. Pokharel and D. A. Lidar, Better-than-classical Grover search via quantum error detection and suppression, *npj Quantum Information* **10**, 1 (2024), publisher: Nature Publishing Group.
- [33] Y. Cao, J. Romero, J. P. Olson, M. Degroote, P. D. Johnson, M. Kieferová, I. D. Kivlichan, T. Menke, B. Peropadre, N. P. D. Sawaya, S. Sim, L. Veis, and A. Aspuru-Guzik, Quantum Chemistry in the Age of Quantum Computing, *Chemical Reviews* **119**, 10856 (2019), publisher: American Chemical Society.

- [34] J. I. Colless, V. V. Ramasesh, D. Dahlen, M. S. Blok, J. R. McClean, J. Carter, W. A. de Jong, and I. Siddiqi, Robust determination of molecular spectra on a quantum processor, *Physical Review X* **8**, 011021 (2018), arXiv:1707.06408 [quant-ph].
- [35] J. I. Colless, V. V. Ramasesh, D. Dahlen, M. S. Blok, M. E. Kimchi-Schwartz, J. R. McClean, J. Carter, W. A. de Jong, and I. Siddiqi, Computation of molecular spectra on a quantum processor with an error-resilient algorithm, *Physical Review X* **8**, 011021 (2018).
- [36] P. O'Malley, R. Babbush, I. Kivlichan, J. Romero, J. McClean, R. Barends, J. Kelly, P. Roushan, A. Tranter, N. Ding, B. Campbell, Y. Chen, Z. Chen, B. Chiaro, A. Dunsworth, A. Fowler, E. Jeffrey, E. Lucero, A. Megrant, J. Mutus, M. Neeley, C. Neill, C. Quintana, D. Sank, A. Vainsencher, J. Wenner, T. White, P. Coveney, P. Love, H. Neven, A. Aspuru-Guzik, and J. Martinis, Scalable Quantum Simulation of Molecular Energies, *Physical Review X* **6**, 031007 (2016).
- [37] W. van Dam, H. Liu, G. H. Low, A. Paetznick, A. Paz, M. Silva, A. Sundaram, K. Svore, and M. Troyer, End-to-end quantum simulation of a chemical system, arXiv preprint arXiv:2409.05835 (2024).
- [38] J. D. Whitfield, J. Biamonte, and A. Aspuru-Guzik, Simulation of Electronic Structure Hamiltonians Using Quantum Computers, *Molecular Physics* **109**, 735 (2011), arXiv:1001.3855 [physics, physics:quant-ph].
- [39] A. Peruzzo, J. McClean, P. Shadbolt, M.-H. Yung, X.-Q. Zhou, P. J. Love, A. Aspuru-Guzik, and J. L. O'Brien, A variational eigenvalue solver on a photonic quantum processor, *Nature Communications* **5**, 4213 (2014), number: 1 Publisher: Nature Publishing Group.
- [40] J. Romero, R. Babbush, J. R. McClean, C. Hempel, P. J. Love, and A. Aspuru-Guzik, Strategies for quantum computing molecular energies using the unitary coupled cluster ansatz, *Quantum Science and Technology* **4**, 014008 (2018), publisher: IOP Publishing.
- [41] R. J. Bartlett, S. A. Kucharski, and J. Noga, Alternative coupled-cluster ansätze ii. the unitary coupled-cluster method, *Chemical physics letters* **155**, 133 (1989).
- [42] A. G. Taube and R. J. Bartlett, New perspectives on unitary coupled-cluster theory, *International journal of quantum chemistry* **106**, 3393 (2006).
- [43] A. Szabo and N. S. Ostlund, *Modern Quantum Chemistry: Introduction to Advanced Electronic Structure Theory* (Courier Corporation, 1996) google-Books-ID: 6mV9gYzEkGIC.
- [44] M. A. Nielsen and I. L. Chuang, *Quantum Computation and Quantum Information: 10th Anniversary Edition* (Cambridge University Press, 2010).
- [45] A. Barenco, C. H. Bennett, R. Cleve, D. P. DiVincenzo, N. Margolus, P. Shor, T. Sleator, J. A. Smolin, and H. Weinfurter, Elementary gates for quantum computation, *Physical review A* **52**, 3457 (1995).
- [46] R. Hicks, B. Kobrin, C. W. Bauer, and B. Nachman, Active readout-error mitigation, *Physical Review A* **105**, 012419 (2022), publisher: American Physical Society.
- [47] A. J. McCaskey, D. I. Lyakh, E. F. Dumitrescu, S. S. Powers, and T. S. Humble, Xacc: a system-level software infrastructure for heterogeneous quantum-classical computing, *Quantum Science and Technology* **5**, 024002 (2020).
- [48] ClaudinoDaniel, M. J, and L. I, A Backend-agnostic, Quantum-classical Framework for Simulations of Chemistry in C++, *ACM Transactions on Quantum Computing* 10.1145/3523285 (2022), publisher: ACMPUB27New York, NY.
- [49] C. Ryan-Anderson, N. C. Brown, M. S. Allman, B. Arkin, G. Asa-Attuah, C. Baldwin, J. Berg, J. G. Bohnet, S. Braxton, N. Burdick, J. P. Campora, A. Chernoguzov, J. Esposito, B. Evans, D. Francois, J. P. Gaebler, T. M. Gatterman, J. Gerber, K. Gilmore, D. Gresh, A. Hall, A. Hankin, J. Hostetter, D. Lucchetti, K. Mayer, J. Myers, B. Neyenhuis, J. Santiago, J. Sedlacek, T. Skripka, A. Slattey, R. P. Stutz, J. Tait, R. Tobey, G. Vittorini, J. Walker, and D. Hayes, Implementing Fault-tolerant Entangling Gates on the Five-qubit Code and the Color Code (2022), arXiv:2208.01863 [quant-ph].
- [50] S. Endo, Z. Cai, S. C. Benjamin, and X. Yuan, Hybrid quantum-classical algorithms and quantum error mitigation, *Journal of the Physical Society of Japan* **90**, 032001 (2021).
- [51] Y. Shee, P.-K. Tsai, C.-L. Hong, H.-C. Cheng, and H.-S. Goan, Qubit-efficient encoding scheme for quantum simulations of electronic structure, *Physical Review Research* **4**, 023154 (2022).
- [52] P. K. Barkoutsos, J. F. Gonthier, I. Sokolov, N. Moll, G. Salis, A. Fuhrer, M. Ganzhorn, D. J. Egger, M. Troyer, A. Mezzacapo, S. Filipp, and I. Tavernelli, Quantum algorithms for electronic structure calculations: Particle-hole Hamiltonian and optimized wave-function expansions, *Physical Review A* **98**, 022322 (2018), publisher: American Physical Society.